

Article

Differential Evolution-Based Overcurrent Protection for DC Microgrids

Miao Li *, Daming Zhang, Shibo Lu, Xiuhui Tang and Toan Phung 

School of Electrical Engineering and Telecommunications, University of New South Wales, Kensington, NSW 2052, Australia; daming.zhang@unsw.edu.au (D.Z.); shibo.lu@unsw.edu.au (S.L.); xiuhui.tang1@unsw.edu.au (X.T.); toan.phung@unsw.edu.au (T.P.)

* Correspondence: miao.li@unsw.edu.au

Abstract: DC microgrids have advantages over AC microgrids in terms of system efficiency, cost, and system size. However, a well-designed overcurrent protection approach for DC microgrids remains a challenge. Recognizing this, this paper presents a novel differential evolution (DE) based protection framework for DC microgrids. First, a simplified DC microgrid model is adopted to provide the analytical basis of the DE algorithm. The simplified model does not sacrifice performance criterion in steady-state simulation, which is verified through extensive simulation studies. A DE-based novel overcurrent protection scheme is then proposed to protect the DC microgrid. This DE method provides an innovative way to calculate the maximum line current, which can be used for the overcurrent protection threshold setting and the relay coordination time setting. The detailed load condition and solar irradiance for each bus can be obtained by proposed DE-based method. Finally, extensive case studies involving faults at different locations are performed to validate the proposed strategy's effectiveness. The expandability of the proposed DE-based overcurrent protection framework has been confirmed by further case studies in seven bus mesh systems.



Citation: Li, M.; Zhang, D.; Lu, S.; Tang, X.; Phung, T. Differential Evolution-Based Overcurrent Protection for DC Microgrids. *Energies* **2021**, *14*, 5026. <https://doi.org/10.3390/en14165026>

Academic Editor: J. C. Hernandez

Received: 6 July 2021

Accepted: 12 August 2021

Published: 16 August 2021

Publisher's Note: MDPI stays neutral with regard to jurisdictional claims in published maps and institutional affiliations.



Copyright: © 2021 by the authors. Licensee MDPI, Basel, Switzerland. This article is an open access article distributed under the terms and conditions of the Creative Commons Attribution (CC BY) license (<https://creativecommons.org/licenses/by/4.0/>).

Keywords: differential evolution; DC microgrid; overcurrent protection

1. Introduction

The traditional way of energy harvesting is inefficient and emission-intensive, which is the culprit for global climate change, extreme weather, and natural disasters. Therefore, the trend to use new environmentally friendly energy resources instead of traditional energy resources is becoming prosperous [1]. Renewable resources such as solar energy, fuel cells, and wind energy are introduced into the energy market as distributed generation (DG) in order to combat greenhouse gas emission. To explore the full potential of renewable energy, a microgrid is proposed to coordinate these distributed energy resources (DER) and renewable energy storage systems (RES) with different loads [2–5], which can operate either in grid-connected mode or isolated mode [6]. Furthermore, the isolated microgrid, also called an islanded microgrid, plays a vital role in supplying power in rural areas and sparse locations.

Recently, the multi-energy microgrids are growing prosperously. Different energy sources are incorporated into this multi-energy microgrid [7,8]. It usually includes an electric system, natural gas, and hydrogen. This multi-energy system has higher efficiency than the single source as the different energy sources in the system can compensate each other [7]. Further, multi-energy systems with more than two different source are gaining more attention as well. The DC microgrid is able to interface DERs, RES, and loads into one common bus, which is becoming much more attractive worldwide. Compared to the AC microgrid, the DC microgrid is more efficient due to its less energy-consuming conversion process which leads to less heat waste [9,10]. There is also no synchronization involved for the DC microgrid, which simplifies the control and optimization process. Furthermore, some disadvantages the AC microgrid has can be conquered by a DC microgrid, such as

power quality enhancement, inrush current of transformer, and reactive power flow [11]. Owing to the RES' utilization, the blackout influence from the primary grid is negligible [1]. Especially for remote areas which are geographically isolated, an independent power source is essential. The independent DC power systems are called islanded DC microgrids [12], and they can reliably provide electricity supply at critical loads [2].

To safeguard DC microgrid operation and promote its widespread installation [13], a comprehensive and well-functioning protection method could drastically increase the reliability, dependability, and security of DC microgrid [14,15]. However, one of the main challenges for DC microgrid protection is detecting fault without the natural zero-crossing point [10,16,17]. In addition, due to the low cable resistance, the fault current increases rapidly, making protection coordination more difficult. To address above challenges, one of the solutions is artificial intelligent based method, which has been drawn attention recently in DC microgrids [18–22]. Although these intelligent methods have been demonstrating promising results, there are still many technical barriers preventing them from being applied to industry such as limited/imbalanced dataset, data inconsistency, and difficulties in cost-effective real-time implementation.

Until now, many protection methods have been studied for DC microgrid. Similar to the AC microgrid, overcurrent protection, differential protection, directional overcurrent protection, distance protection, and current derivative protection methods have gained much attention [16]. A protection method for the DC ring bus system is described in [23], which is based on the parameters measured locally. Distance protection can be applied to DC microgrids as well. The distance information can be obtained by measuring from the checking point to the faulty point. If the value of impedance falls into the operation zone, the fault will be detected. In [24], the local measurement-based method was utilized to protect the DC microgrids as well. The integral and derivative of current values are used to detect the fault. In [25], Yang et al. proposed a method by analyzing circuit and adopting iteration calculation. However, the error is dependent on the fault resistance, which reduces the reliability of this algorithm. The impedance between the checking point and the faulty point can also be measured by employing the filters and extra sensors, which was discussed in [26]. It can avoid weakness of a communication system. However, the cost of this method is relatively high compared to the method proposed in [25]. As for the high impedance and a small part of the cable, this method has lower accuracy. Jia et al. in [27] discussed a new back-up protection method using transient current correlation to set the threshold.

Overcurrent-based protection strategies and differential protection strategies are the main choices for the DC microgrid [28]. In [29,30], differential protection methods by measuring the current on each side of the feeder had been discussed. A protection method using differential protection and discrete wavelet transform was proposed in [31]. However, the synchronization and communication between the measurement unit and the control center may lead to the data transfer delay. In [32], Reis et al. discussed the current derivative-based protection method. This method is based on the increasing speed of the fault current. Augustine et al. in [33] proposed current derivative protection combined with adaptive droop control to lower the fault current and explain the way to define the current derivative threshold. Compared to other overcurrent-based protection methods, more sensors with high sampling frequency need to be installed in the microgrid, which significantly increases the noise and possibilities to get maltrip. Moreover, the threshold for the high current derivative is also difficult to be set. Based on the overcurrent protection, both fault current and its direction were considered in [34,35]. These kinds of methods demonstrate better selectivity and reliability than overcurrent protection. However, the renewable energy systems that exert significant influence on the DC microgrids were not taken into account in these papers. Most importantly, the detailed way to set the pick-up current threshold was not discussed thoroughly in existing papers, and effective methods are yet to be developed. In [2,36], authors proposed overcurrent protection method for DC microgrid. The fault current is compared with the tripping threshold set for detection.

When the fault current is over the limit, the overcurrent protection scheme is triggered. However, it is not clear whether this setup is suitable for detecting different types of fault and identifying load changes; they are mainly dependent on the threshold, devices, and architecture, which reduce the robustness of the system. If DC microgrid has a complex architecture, the coordination time would be longer, and the elimination of the fault could cause the large-scale disconnection. It is essentially important for the overcurrent protection to determine the maximum line current accurately to have proper pick-up current setting and such a target has not been fully achieved by the papers reviewed above. Although Shabani et al. in [28] discussed using maximum line current, the detailed way to acquire the maximum operation current was not fully expressed.

To overcome the difficulties of setting threshold for the overcurrent protection, a novel differential evolution (DE) based framework has been proposed. In this framework, the simplified model has been adopted to simulate the complex model's steady-state response. Furthermore, the DE algorithm has been first utilized to obtain the maximum line current based on the simplified model. Then, the new way to calculate the pickup current for overcurrent protection has been investigated through a four-bus system with ring configuration. The extendability has been discussed by making use of the seven-bus system with mesh configuration. The proposed framework has been developed after all power resources have been connected to each bus. The black start condition will not be considered in this case.

The remaining parts of the paper are organized with following sequence. Section 2 discusses the procedure of obtaining the simplified model in great detail. The simplified model and complex model are proven to be consistent in steady state results in Section 3. At the same time, the extensive case studies have been conducted to validate the feasibility of proposed DE protection framework. Conclusion and remarks on the protection method and the simulation results have been drawn in Section 4.

2. The Simplified DC Microgrid Model

Instead of simulating the DC microgrid using a complex model, a simplified model is adopted to establish the steady-state analysis for DC microgrids. For different DGs, they can be converted to the simple models separately. Based on the interconnection of the single bus, the whole DC microgrid model can be simplified.

2.1. DC Microgrid System Complex Model Configuration under Conversion

An islanded ring-type DC microgrid is built to design the protection method shown in the Figure 1. Compared to other topologies, the ring bus topology is a highly reliable [37]. This DC microgrid contains two Photovoltaic (PV) systems and two battery systems. There are two units in each PV system: PV arrays (modeled by SunPower SPR-305E-WHT-D model provided by Matlab/Simulink) and one bidirectional boost converter. The Perturb and Observe (P&O) control method is adopted to obtain the maximum power. For battery system, it consists of battery units and a boost converter. The parameters for the DC microgrid are summarized in Table 1. In addition, Table 2 presents the detailed parameters for the PV array model used in Matlab/Simulink.

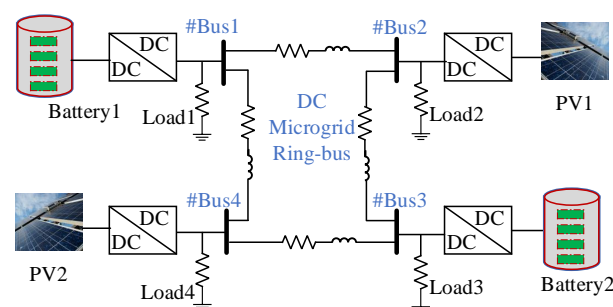


Figure 1. Four-bus DC microgrid with ring configuration.

Table 1. DC Microgrid Configuration Parameters.

Name	Values
PV System MPP	100 kW
Cable resistance	0.9 Ω /kM
Bus voltage	700 V
Cable inductance	0.334 mH/kM
Series-connected modules per string in PV panel	5
Parallel strings in PV panel	66

Table 2. SunPower SPR-305E-WHT-D model data.

Parameter per Module	Value	Parameter per Module	Value
Maximum power	305.2 W	Cell per module	96
Voltage at MPP	54.7 V	Current at MPP	5.58 A
Short-circuit current	5.96 A	Open circuit voltage	64.2 V

2.2. Simplified Model

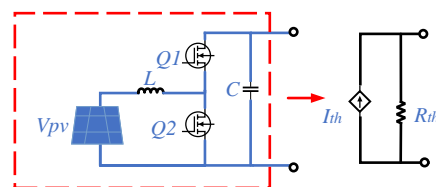
2.2.1. PV System Model

As discussed in the previous section, the PV system needs to be operated at the maximum power point (MPP), which is affected by varying solar irradiance and temperature [38]. Thus, a maximum power point tracking (MPPT) technique is applied [38]. Furthermore, if the operating point is off track, MPPT must quickly react to any unprecedented conditions and regulate the PV system back to MPP.

During the conversion process, it is assumed the PV system operates at MPP at all times at a certain irradiance level. The applied voltage control system ensures the PV system's output voltage is the same as the constant bus voltage. As a result, the output current can be derived from the maximum power and the bus voltage. The expression can be shown as follows:

$$I_{pv} = P_{pv} / V_{dc} \quad (1)$$

where I_{pv} denotes the output current of the PV system, P_{pv} stands for the total maximum power of the PV system, and V_{dc} is the DC bus voltage. Considering that the MPP is affected by varying environmental conditions, the PV system output current is regarded as a controlled current source. Thus, PV system output can be simplified as a controlled current source connected in parallel with a resistance shown in Figure 2. R_{th} in Figure 2 is the total output equivalent resistance for the PV system.

**Figure 2.** The equivalent circuit for PV system.

2.2.2. Battery System Model

The role of the battery storage system is to keep the DC bus voltage at a certain level, which improves power sharing between different resources. The battery system will inject more power into the microgrid when other resources are not generating enough power to meet the microgrid's electricity demand. Otherwise, the extra energy generated is diverted into battery system. At the same time, cascade control is used to stabilize the output voltage and output current at a certain level. In addition, droop control is

applied to achieve equal power sharing of the batteries, and to distribute power to different battery systems. The droop control used in this paper is voltage droop control. Thus, by combining cascade control with voltage droop control, the battery can be treated equally as a controllable voltage source with an internal resistance shown in Figure 3. Due to the power sharing function, the output voltage of the battery in Figure 3 can be expressed by the equation showing below:

$$V_{bat} = V_{ref} - droop \cdot I_{line} \quad (2)$$

where V_{bat} denotes the terminal voltage of battery system, V_{ref} denotes the required DC bus voltage, $droop$ is the droop coefficient of droop control for each battery system, and I_{line} is bus current fed into battery system. In Matlab/Simulink, a controlled voltage source is adopted to represent the simplified battery model. In Figure 3, R_{th} is the total output equivalent resistance of battery system, and V_{th} is the output voltage of battery system.

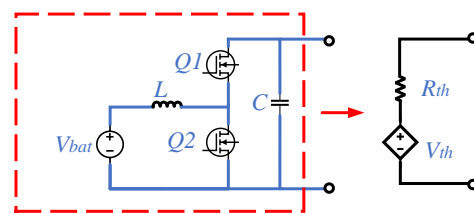


Figure 3. The equivalent circuit for battery system.

2.3. Current Flow Analysis

In an N -bus system, there are x buses with PV systems, y buses with battery systems, and $N - x - y$ pure loads. To analyze the system load flow, it is necessary to obtain the expression for each line current. The line currents can be derived by determining bus voltages by the following matrix:

$$I_{source} = Y_{bus} \times V_{bus} \quad (3)$$

where I_{source} denotes equivalent current source at each bus, Y_{bus} means the admittance matrix of the system and V_{bus} stands for the bus voltage matrix. For this N -bus system, the admittance matrix Y_{bus} can be obtained as follows:

$$Y_{bus} = \begin{bmatrix} Y_{1,1} & Y_{1,2} & \cdots & Y_{1,N} \\ Y_{2,1} & Y_{2,2} & \cdots & Y_{2,N} \\ \vdots & \vdots & \ddots & \vdots \\ Y_{N,1} & Y_{N,2} & \cdots & Y_{N,N} \end{bmatrix} \quad (4)$$

The diagonal elements $Y_{i,i}$ of the Y_{bus} stand for the self admittance for each node. It can be expressed as

$$Y_{i,i} = y_{i,i} + \sum_{j=1}^N y_{i,j}, (i \neq j). \quad (5)$$

where $y_{i,i}$ stands for the all the self admittance connected to the reference node i . $i = 1, 2, 3, \dots, N$ denotes the index of nodes. The off-diagonal components $Y_{i,j}$ denote the mutual admittance between two nodes i and j , and their values should be negative. As shown in Figure 1, there is a local load connecting to each node, therefore, its contribution to the respective diagonal element can be expressed as $1/R_{load,i}$. The diagonal element expression is shown as

$$Y_{i,i} = 1/R_{load,i} + \sum_{j=1}^N y_{i,j}, (i \neq j). \quad (6)$$

$$Y_{i,j} = -y_{i,j}, (i \neq j). \quad (7)$$

Based on the simplified model mentioned in the previous part, a PV system can be simplified as a controlled current source, which means that the output current of the whole PV system is known. The battery system can be evaluated as a controlled voltage source, which defines the output voltage of the battery source. Based on the droop coefficients used, the output voltage of battery system can be derived.

The bus voltage is expressed as Equation (8):

$$V_{bus} = [V_1, V_2, \dots, V_i, \dots, V_N]^T \quad (8)$$

For the i th bus voltage, if it is a battery system, the voltage can be expressed as

$$V_{bat_i} = V_{ref} - droop \cdot I_{bat_i} \quad (9)$$

If the i th system is a pure load, voltage can be derived as

$$V_{load_i} = I_{load_i} \cdot R_{load_i} \quad (10)$$

Furthermore, the bus current can be expressed as

$$[I_1, I_2, \dots, I_i, \dots, I_N]^T \quad (11)$$

If i th system is a PV system, I_i can be revealed as

$$I_{pv_i} = P_{pv_i} / V_{ref} \quad (12)$$

Taking Equation (8) to Equation (12) together, bus voltage can be gained.

Then, after obtaining the bus voltage, the line current can be calculated as follows:

$$I_{i,j} = (V_i - V_j) \times y_{i,j} \quad (13)$$

where $I_{i,j}$ denotes the current flows from bus i to bus j . If the current flows from bus j to bus i , it can be expressed as $I_{j,i} = -I_{i,j}$.

2.4. Differential Evolution

DE is one of the most popular optimization methods widely used in different engineering fields [39], especially in those fields which need to solve stochastic and optimized problems. DE has many advantages that support its popularity, such as simplicity in its codes, lower space complexity, a smaller number of control parameters and its robustness [40]. The aim of DE is to find out the best parameters under some certain situations with specified constraints.

The number of individual included in the population of DE is NP . Each individual can be expressed as vector X with D dimensions [41]:

$$X_i^G = \{x_{i,1}^G, x_{i,2}^G, x_{i,3}^G, \dots, x_{i,D}^G\} \quad (14)$$

where i denotes the solution in G th generation, $i = 1, 2, \dots, NP$. $G = 0, 1, \dots, G_{max}$ stands for the generations in DE.

The main steps of DE includes initialization, mutation, crossover, and selection. The initialization vectors are randomly defined by some restraints, which usually have their natural limits. The $X_{low} = \{x_{low,1}, \dots, x_{low,D}\}$ and $X_{high} = \{x_{high,1}, \dots, x_{high,D}\}$ are the prescribed minimum and maximum parameter limits. The first vector should contain elements as many as possible, which widens the searching range. Then, the initial j th components of i th vector at initial generation ($G = 0$) are defined by

$$x_{i,j}^0 = x_{low,j} + rand \times (x_{high,j} - x_{low,j}) \quad (15)$$

where *rand* stands for the uniformly random distributed parameters and its range is $0 \leq rand \leq 1$.

After initialization process is completed, the mutation operation starts. The disturbance is added to the target vector. The donor vector can be expressed as follows:

$$V_i^G = X_{r_1,i}^G + F \times (X_{r_2,i}^G - X_{r_3,i}^G) \quad (16)$$

where r_1, r_2 , and r_3 indicate the random numbers selected among population within the range of $[1, NP]$ [42], and F is the positive scaling factor aiming to scaling the difference vector [43].

To enrich the diversity of population, the trial vector $U_i^G = (u_{i,1}^G, u_{i,2}^G, u_{i,3}^G, \dots, u_{i,D}^G)$ has been generated by applying crossover to each pair of the target vector X_i^G and its related mutant vector V_i^G . The trial vector elements are obtained by extracting variables from $v_{i,n}^G$ and $x_{i,n}^G$.

$$u_{i,n}^G = \begin{cases} v_{i,n}^G & \text{if } (rand_n[0, 1] \leq C_r \text{ or } n = n_{rand}). \\ x_{i,n}^G & \text{otherwise } j = 1, 2, \dots, D \end{cases} \quad (17)$$

where C_r denotes the crossover rate within the range $[0, 1)$ functioning as the scalar control parameters for controlling the fraction of parameter values copied from the mutant vector. $u_{i,n}^G$ is the n th elements of the i th choice in generation G . n_{rand} is the integer in the range of $[1, D]$ selected randomly [43].

The last operation step of DE is selection. The main purpose of selection is to filter unqualified target vector or trial vector to the next generation. $f(\cdot)$ is the objective function to be minimized. Based on following formula, the operation can be conducted [44].

$$X_i^G = \begin{cases} U_i^{G-1}, & \text{if } f(U_i^{G-1}) \leq f(X_i^{G-1}). \\ X_i^{G-1}, & \text{otherwise.} \end{cases} \quad (18)$$

After the initialization, the iteration operation steps from mutation to selection, and the processing stops until the ceasing criteria has been fulfilled.

In this paper, the purpose of using DE is to acquire the largest line current. Then, the objective function set for this paper would be $f(I_{line}) = 1/I_{line}$. The aim of the optimization is to minimize the value of $1/I_{line}$. When $1/I_{line}$ reaches its smallest value, the value of I_{line} becomes the largest, which is the required worst case line current value.

The parameters set for the initial population are loads of different systems and output current of PV system. The output current at MPP shows the different irradiance under dissimilar weather conditions. Suppose both PV systems work under MPP due to the effective MPPT method, the lower boundary set for PV irradiance is one-tenth of the maximum irradiance, which corresponds to $0.1I_{pv, stc}$. $I_{pv, stc}$ denotes PV current under standard test condition which is 25°C , 1000 W/m^2 . 0.1 of $I_{pv, stc}$ simulates the cloudy day which has little sunshine. The upper boundary set for PV irradiance is the maximum irradiance referring to the $I_{pv, stc}$.

The overall algorithm framework flowchart is shown in the Figure 4.

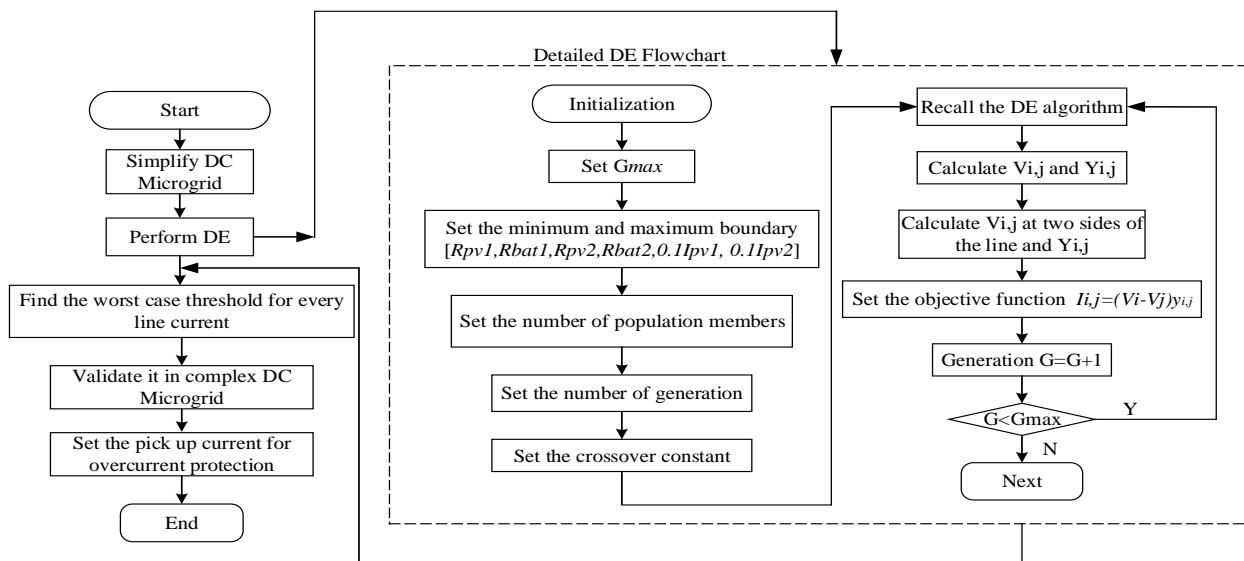


Figure 4. The proposed framework of algorithm.

3. Case Study

3.1. Verification of The Simplified Model

In previous sections, the processes of acquiring equivalent circuits of PV system and battery system have been discussed respectively. Both complex and simplified models are verified and compared by simulation in Matlab/Simulink in this section.

The same parameters should be set for both models to ensure their results are comparable. A comparison of output voltage, output current, and output power of the PV system and battery system can be used to check the consistency between two models.

The comparison results of PV system for complex model and simplified model are shown in the Figures 5 and 6. It can be clearly seen that the output results for complex model and simplified model are in consistence with each other. Although there are fluctuations occurring in system output response, the output current and voltage of simplified model is close to the average output current and voltage of complex model.

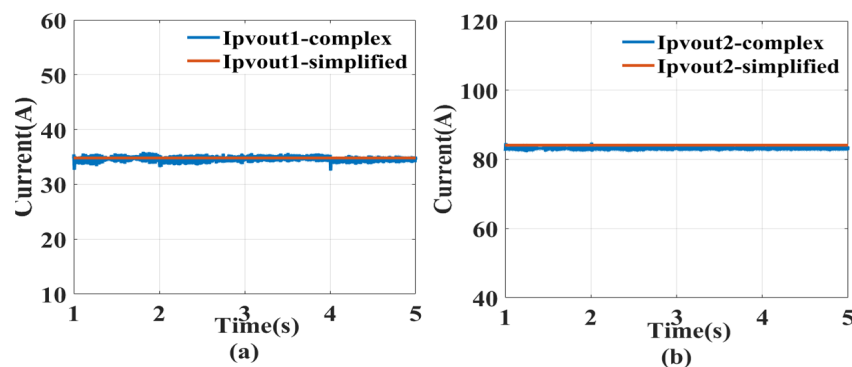


Figure 5. The output current comparison of PV system: (a) the comparison for PV system 1 and (b) the comparison for PV system 2.

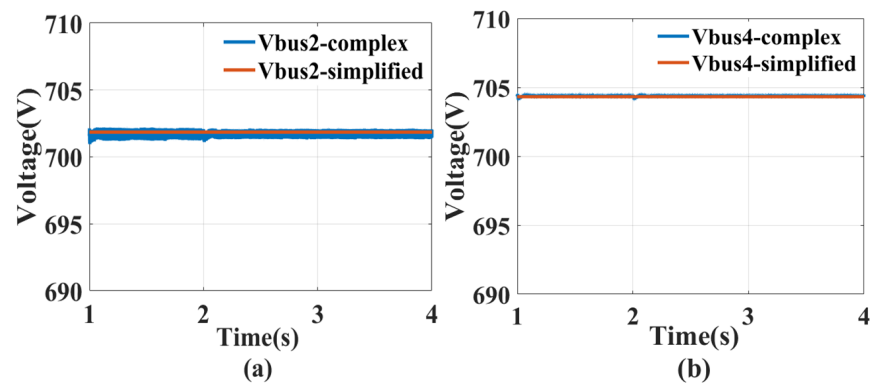


Figure 6. The bus voltage comparison for Bus 2 and Bus 4, which are connected to PV systems: (a) the comparison for Bus 2 and (b) the comparison for Bus 4.

Figures 7 and 8 show the comparison results between complex models and simplified models. Compared to PV system outputs, the output voltage and current of battery systems from two different models are nearly the same as well.

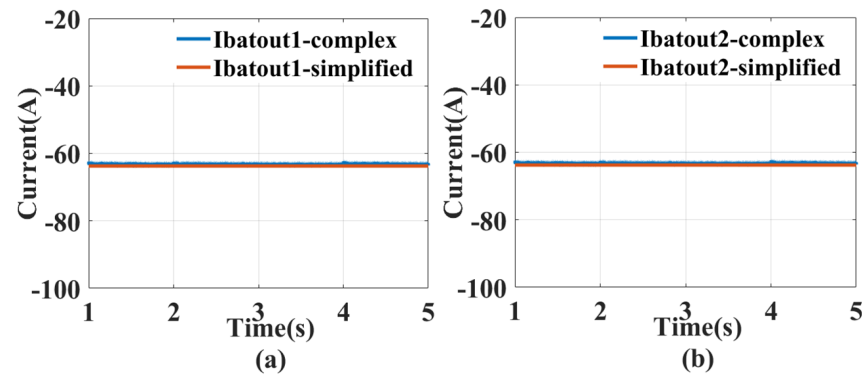


Figure 7. The output current comparison for battery system: (a) the comparison for battery system 1 and (b) the comparison for battery system 2.

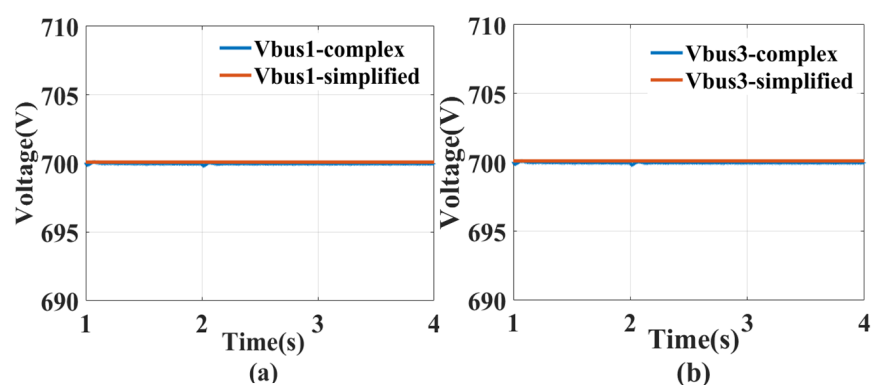


Figure 8. The bus voltage comparison for Bus 1 and Bus 3, which are connected to battery systems: (a) the comparison for Bus 1 and (b) the comparison for Bus 3.

Table 3 further describes detailed output current values and errors between different simulation models. The line current errors under different loading levels between different models are less than 1%.

Table 3. The comparison results for line current.

Model Type	I_{line}							
	Loading 1				Loading 2			
	Bat_1	Bat_2	PV_1	PV_2	Bat_1	Bat_2	PV_1	PV_2
Simplified Model	−63.7	−63.7	63.7	63.7	−59.3	−59.3	34.8	84.1
Complex Model	−63.3	−63.3	63.5	63.5	−58.5	−58.5	34.5	83.5
Error	0.6%	0.6%	0.3%	0.3%	1%	1%	0.8%	0.7%

From Table 4, the voltage errors between two models are less than 0.15% under various load conditions. In summary, from Figures 5–8 and Tables 3 and 4, it can be demonstrated that the simplified model and complex model are consistent in steady state. In other words, the simplified model is effective and accurate to simulate the steady state of complex model.

Table 4. The comparison results for output voltage.

Model Type	V_{out}							
	Loading 1				Loading 2			
	Bat_1	Bat_2	PV_1	PV_2	Bat_1	Bat_2	PV_1	PV_2
Simplified Model	700	700	703	703	700	700	702	704
Complex Model	700	700	704	704	700	700	702	704
Error	0	0	0.14%	0.14%	0	0	0	0

3.2. Power Flow Calculation Using Differential Evolution

In this section, the proposed whole framework using DE is analyzed and the case studies using two different DC microgrid configurations are presented.

3.2.1. Four-Bus Ring System

The configuration of four-bus system used in this section is shown in Figure 1. To use the DE to calculate the maximum line current, the objective function can be set as the function of I_{line} . The way to get the line current can be concluded as following equations:

$$\begin{cases} [I_{bat1}, I_{pv1}, I_{bat2}, I_{pv2}]^T = Y_{bus} \times [V_{bat1}, V_{pv1}, V_{bat2}, V_{pv2}]^T \\ V_{bat1} = V_{ref} - droop_1 \cdot I_{bat1} \\ V_{bat2} = V_{ref} - droop_2 \cdot I_{bat2} \\ I_{pv1} = P_{pv1} / V_{ref} \\ I_{pv2} = P_{pv2} / V_{ref} \end{cases} \quad (19)$$

where

$$Y_{bus} = \begin{bmatrix} Y_{1,1} & Y_{1,2} & Y_{1,3} & Y_{1,4} \\ Y_{2,1} & Y_{2,2} & Y_{2,3} & Y_{2,4} \\ Y_{3,1} & Y_{3,2} & Y_{3,3} & Y_{3,4} \\ Y_{4,1} & Y_{4,2} & Y_{4,3} & Y_{4,4} \end{bmatrix} \quad (20)$$

Then, the current for each line can be expressed as

$$\begin{cases} I_{1,2} = (V_{bat1} - V_{pv1}) \cdot y_{1,2} \\ I_{2,3} = (V_{pv1} - V_{bat2}) \cdot y_{2,3} \\ I_{3,4} = (V_{bat2} - V_{pv2}) \cdot y_{3,4} \\ I_{4,1} = (V_{pv2} - V_{bat1}) \cdot y_{4,1} \end{cases} \quad (21)$$

To figure out which load conditions and PV irradiance circumstances lead to the largest line current, all possible loads and irradiance conditions should be considered when

defining the constraints factor for DE. To be realistic, the range of loads can be set from the smallest value to the largest value. The other constraint, which is irradiance-level-determined PV unit output current, needs to be set from $0.1I_{pv, stc}$ to $I_{pv, stc}$. This range nearly covers all the possible sunshine conditions. Then, by calling the DE program, the largest line current can be obtained.

Figure 9 shows the DE simulation results for four-bus system. For this four-bus system, nearly all maximum line currents have similar values. Note that the maximum line current value of the same line is not identical for different directions. For instance, the maximum line current value for $I_{3,4}$ and $I_{4,3}$ are 63.28 A and 64.41 A, respectively. That is because the loading condition, PV operation situation, and the battery operation condition are different for different directions of line current.

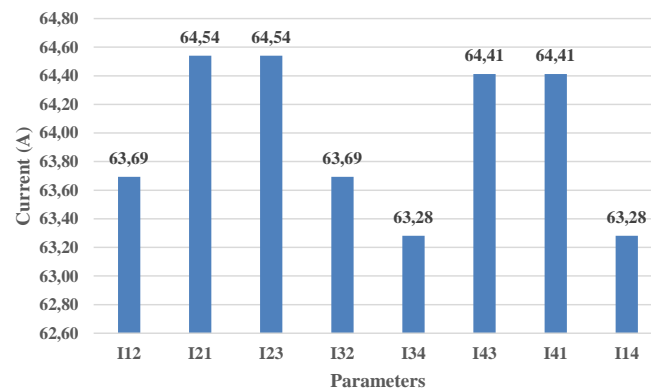


Figure 9. The DE simulation results for four-bus system.

3.2.2. Seven-Bus Mesh System

The configuration of seven-bus mesh-type DC microgrid is shown in the Figure 10. It contains three PV systems, three battery systems, and one load unit. Based on the Y-bus calculation and DE evolution methods described in previous part, the maximum line current can be derived.

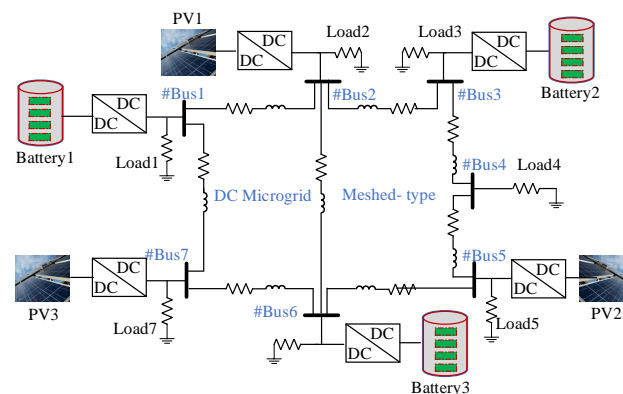


Figure 10. Seven-bus meshed-type DC microgrid configuration.

The DE results for seven-bus system are shown in Figure 11. This figure shows that the maximum line currents are quite different compared to four-bus system's results. Especially, $I_{3,4}$, $I_{5,4}$, and $I_{6,5}$ are much larger than other line currents. Furthermore, currents flowing through the line connected to the pure load system are also higher than other line currents. This is because bus 4 is connected to the pure load system which can consume more current, if it were at the worst case. The average DE algorithm computation time is 2.834 s in 30 runs, and its time complexity is $O(n^2)$. All the simulation experiments are carried out on the PC with CPU processor is Intel (R) Core (TM) i7-8750H CPU @2.20 GHz with 32 GB RAM.

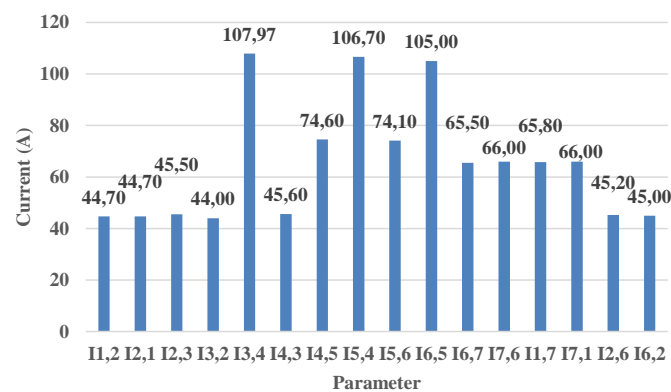


Figure 11. The DEsimulation results for seven-bus system.

3.3. Protection Issues Case Study

The traditional way to set pick-up current for the overcurrent protection is to use the current, I_{op} , at the rated loading condition [33,45]. Then, pick-up current is set as 1.2–1.5 I_{op} . However, for the microgrid, the situation becomes more complex with renewable resources present, such as PV systems and battery systems. The PV system output is affected by different sunshine irradiance and temperature, introducing unprecedented power flow fluctuations. The output of PV generation systems can influence battery energy allocation as well. All these stochastic factors have exerted an influence at microgrid operation condition. The worst-case scenario is widely used to calculate the largest line current. However, it is difficult to determine which scenario the worst case is. Even though all loads can be under the full load condition, its sunshine condition may also affect the largest line current.

In order to combat the challenge mentioned above, the overcurrent protection threshold can be set by maximum line current obtained by DE. To verify the effectiveness and wide applicability of the proposed DE-based overcurrent protection framework, various scenarios need to be taken into account, including different faults with different fault resistances occurring at various locations. The rest of the paper uses $Line_{3,4}$ as an example for a four-bus system and $Line_{6,7}$ as an example for a seven-bus system. Fault resistances are selected as 1 Ω , 5 Ω , and 10 Ω . In addition, fault locations are set from 5%, 30%, 60%, 75%, and 95% of $Line_{3,4}$ and $Line_{6,7}$.

The loading condition of the four-bus ring microgrid is shown in the Table 5.

Table 5. Loading condition for four-bus ring-type system.

Systems Power	PV_1	PV_2	Bat_1	Bat_2
Power _{max}	100 kW	100 kW	100 kW	100 kW
Power _{min}	10 kW	10 kW	10 kW	10 kW

3.3.1. Fault Occurs at Different Locations of Transmission Line

Faults occurring at different locations will exert different influences on the fault current, which will further influence the overcurrent threshold setting. In this case, faults occurring at different locations will be investigated to demonstrate the feasibility of the algorithm. The starting point of the line is from bus (N) to bus ($N + 1$), where $1 \leq N \leq 3$. That means 5% in the Figure 12 denotes the fault occurs at the location which is 5% of $Line_{3,4}$. Likewise, 30% of the $Line_{3,4}$ means 30% length of $Line_{3,4}$ starting from bus 3. The tested location information is shown in Figure 12 separately.

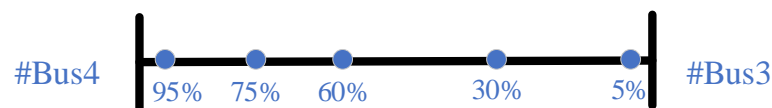


Figure 12. The line length.

The value calculated by DE illustrated in Figure 9 is $I_{3,4} = 63.28$ A. Therefore, $1.2 \times I_{3,4} = 1.2 \times 63.28 = 75.94$ A is set as threshold to judge whether the fault is occurred. In this case, the load condition is 70% of rated load. Figure 13 shows the comparison between the different threshold setting conditions. From Figure 13, the fault current increases with the rise of faulty line length. The normal current is even larger than $1.5I_{op}$. However, the threshold setting by $I_{linemax}$ (obtained by the proposed DE-based method) is beyond normal current showing under normal condition, the system will work normally. Further, this threshold is smaller than the fault current which can successfully lead to the tripping of relay. It is clear that for different situations, the thresholds acquired from DE-based method can detect the fault successfully.

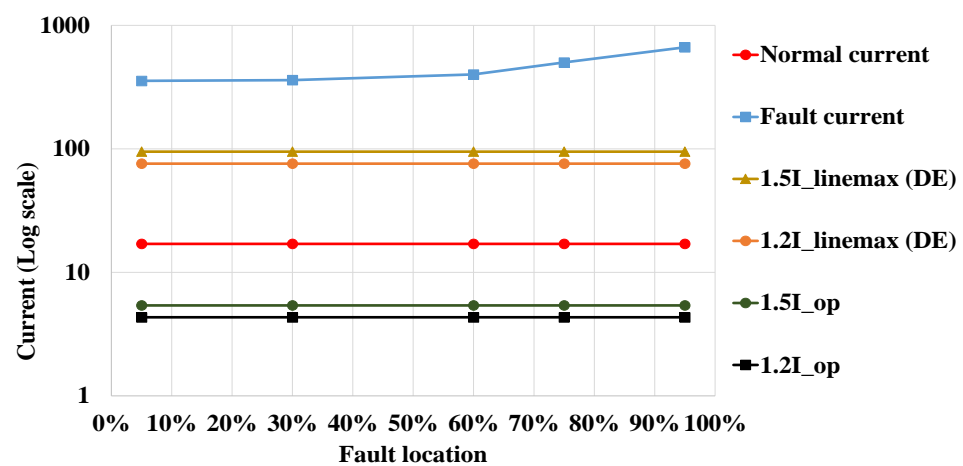


Figure 13. Fault condition at different locations with 70% load and 1Ω fault resistance.

3.3.2. Fault Occurs under Different Load Conditions

In the DC microgrid, varying load conditions may cause different power flow situations. The direction of current flow and the fault current magnitude changes accordingly. The detailed simulation on different faults at different fault location under distinct loading condition has been conducted. It is found that the proposed DE-based overcurrent protection can effectively protect the DC microgrid. Take 1Ω fault which occurs at 95% of the $Line_{3,4}$ under 20%, 50%, 70%, and 90% of the load conditions as examples, and the results are shown in Figure 13.

From Figure 14, the normal line current will decrease with load increasing. In other words, when local load is reaching its maximum load, the current flowing through the transmission line will significantly reduce, owing to the power consumption by the local loads. Note that in Figure 14, the normal current is nearly equal to $1.5I_{op}$, which means when the load is larger than 90% of maximum load, the $1.5I_{op}$ can be used to detect fault as well. However, the threshold is not suitable for any other load condition. To summarize, the proposed threshold setting method using $I_{linemax}$ is fit for every loading condition; $1.5I_{op}$ cannot meet requirements for all situations, but only satisfy a small portion of situations. Thus, to cover all conditions, $I_{linemax}$ setting is adopted.

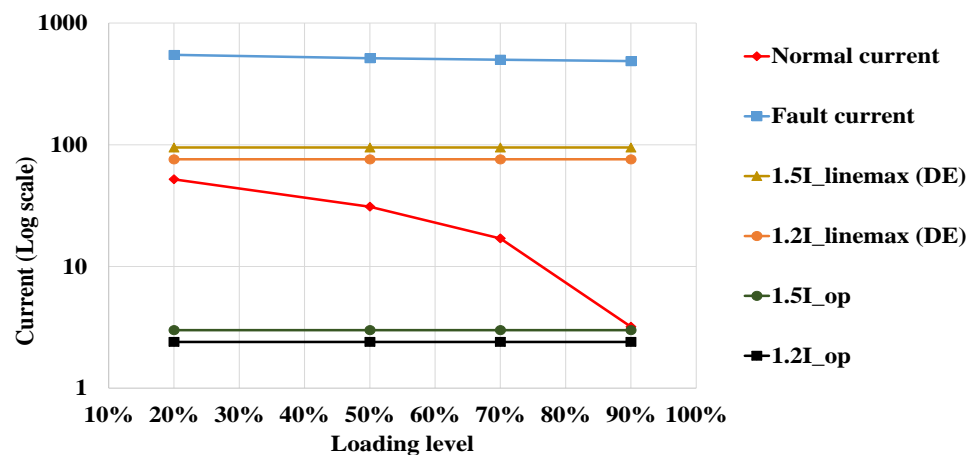


Figure 14. Fault condition under different loading levels with 95% of line and 1Ω fault resistance.

3.3.3. Fault with Different Resistances Occurs at Certain Load Condition

One impacting factor of the system operation situation is the fault resistance. The different fault resistance values exert different influences on system response. An increasing fault resistance is more difficult to detect. To demonstrate the feasibility of the DE-based method to find maximum line current, the different fault resistances are tested. Figure 15 shows the results of 1Ω , 5Ω , and 10Ω occurring at 95% of the line, respectively, under 70% of loading level, which is used to explain the proposed DE-based framework. From Figure 15, fault resistance and fault current are negative related. When the fault resistance is 10Ω , fault current will fall below the threshold $1.5I_{linemax}$, but it is still beyond $1.2I_{linemax}$. Besides, for both $1.2I_{op}$ and $1.5I_{op}$, the normal current is larger than them, which can cause maltrip even when system is under normal condition. As a result, $1.2I_{linemax}$ works for all fault resistances.

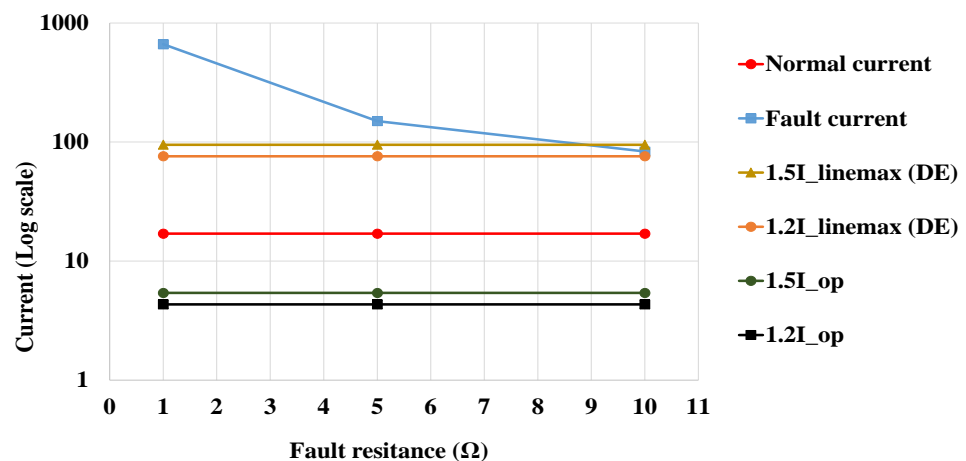


Figure 15. Fault condition with different fault resistances with 70% load and 95% of line.

3.4. Seven-Bus Mesh System

To validate the expandability of DE-based overcurrent protection framework, a study of the seven-bus meshed system has been carried out. Similar tests for four-bus system will be taken on seven-bus system. The results of different faults occur at different locations with different fault resistances are listed in following parts.

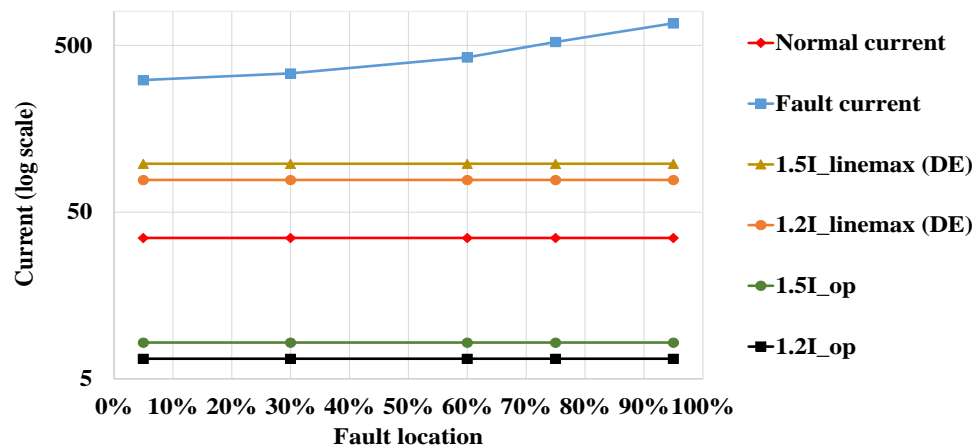
Table 6 shows the detailed loading conditions of the seven-bus mesh system. In this case, the fault is assumed to occur on $Line_{6,7}$, which is the interface of PV system and battery system. This setting is same as four-bus system's. Moreover, this location can fully stand for the special situation when both different types of power system affect each other closely.

Table 6. Loading condition for the seven-bus mesh system.

Systems	Power	Power _{max}	Power _{min}
$PV_i = 1, 2, 3$		100 kW	10 kW
$Battery_i = 1, 2, 3$		100 kW	10 kW
Pure Resistance Branch		100 kW	10 kW

3.4.1. Fault Occurs at Different Locations of Transmission Line

The fault simulation is carried out in the seven-bus mesh system in the same way demonstrated for the four-bus ring system. The simulation results also show the effectiveness of the proposed framework. The results of 1Ω fault occurs on different parts of $Line_{6,7}$, which are 5%, 30%, 60%, 75%, and 95% of $Line_{6,7}$ under 70% of load are listed to explain the proposed framework. Figure 16 shows that comparison results are similar to the results got from four-bus system. Normal current is larger than the tradition overcurrent threshold setting. However, the settings with $I_{linemax}$ work for all different fault locations.

**Figure 16.** Fault condition at different locations with 70% load and 1Ω fault resistance.

3.4.2. Fault Occurs under Different Load Conditions

In this scenario, the proposed framework has been analyzed under different conditions. The simulation results of 1Ω fault that occurs under different loading conditions, such as 20%, 50%, 70%, and 90% of rated load at the 95% of the line are tabulated to explicate the proposed framework. Based on Figure 17, it is clearly shown that fault current changing trend is same as four-bus system. Under this circumstance, traditional way of using rated current to set threshold will trip even when it is under normal operation. In addition, $1.2I_{linemax}$ and $1.5I_{linemax}$ works for all fault location in this scenario.

3.4.3. Fault with Different Resistances Occurs at Certain Load Condition

Different fault resistance values can exert different influences at the system operation. The case has been listed in Figure 18 to analyze the adequacy of DE-based overcurrent protection. The examples took among all the simulation results are 1Ω , 5Ω , and 10Ω occurring at 95% of the line under 70% load. In this case, normal current is still upon the threshold setting by the rated current. If the threshold is set by either $1.2I_{op}$ or $1.5I_{op}$, the relay will trip under normal operation. In addition, the fault current faults falls between $1.5I_{linemax}$ and $1.2I_{linemax}$. This implies that $1.5I_{linemax}$ is too high for relay to detect the fault occurrence. Therefore, $1.2I_{linemax}$ should be selected as the threshold.

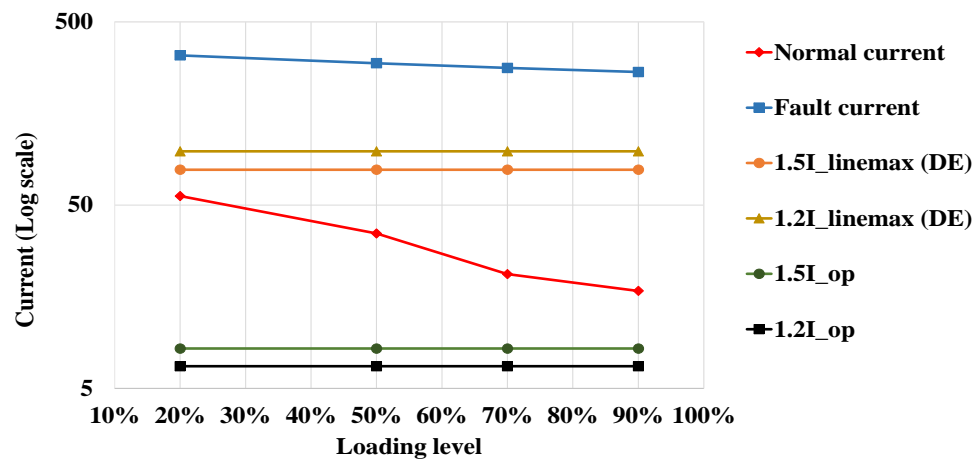


Figure 17. Fault condition under different loading levels with 95% of line and 1 Ω fault resistance.

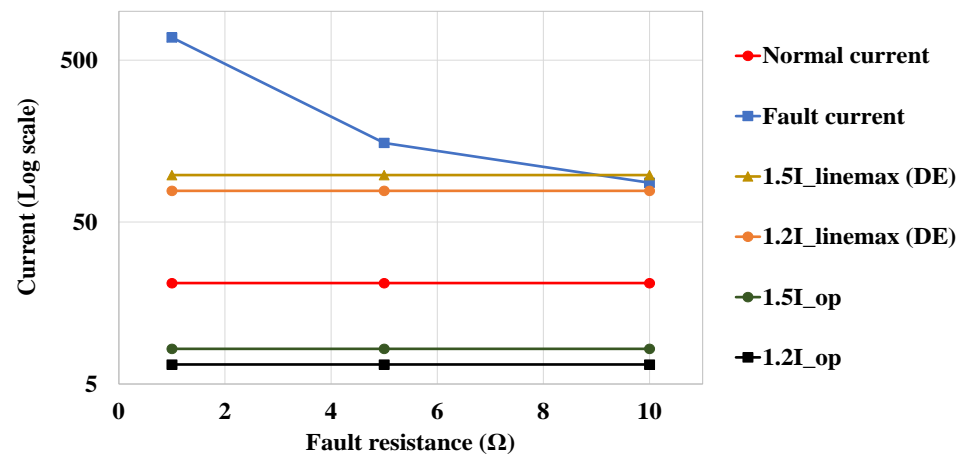


Figure 18. Fault condition with different fault resistances with 70% load and 95% of line.

3.5. Discussion

The proposed DE-based overcurrent protection framework has been tested in a four-bus ring system and a seven-bus mesh system, respectively, with realistic, complex loading levels and operation conditions. The results obtained from the case studies of different DC microgrid systems have a similar trend and show the absolute fault current increases with the loading level decreasing. In addition, whenever the fault occurs nearer the bus-bar, the fault current becomes smaller. Moreover, the fault resistance is inversely proportional to the absolute value of the fault current. Although the threshold setting by the operating current can also detect the fault when the load is over 90% of rated load, the threshold set by $I_{linemax}$ should be selected to meet all requirements for all cases. However, the fault current is below $1.5I_{linemax}$ when fault resistance is 10 Ω . That implies $1.5I_{linemax}$ is only effective when system has fault with low resistance. Therefore, $1.2I_{linemax}$ should be selected as the threshold for overcurrent protection in the proposed framework for all cases. Compared to the overcurrent protection scheme presented in [28], the protection whole framework proposed in this paper shows the detailed methodology to calculate the maximum line current. The described protection method in [46] did not consider the fault occurring under different load conditions, while the fault occurs at different locations with different loading conditions has been fully discussed in this paper.

4. Conclusions

In conclusion, this paper proposes a framework combining differential evolution with an overcurrent protection scheme to effectively protect the system. The details of designing this framework have been discussed. In this framework, a simplified model was used to

replace a complex model of the DC microgrid to simulate its steady state. The voltage errors between two different models are less than 0.2%, while line current errors are less than 1%. The low error implies that the simplified model is effective and accurate in steady states. Based on the simplified model, matrix equation $[Y][V] = [I]$ together with controlled current source model for PV array and controlled voltage source for battery had been obtained. Variation of solar irradiance and load levels were taken into consideration as well. This provided a mathematical model to calculate the current flowing from the each line. In differential evolution algorithm, reciprocal of line current was set as an objective function. Then maximum line current for each transmission line can be obtained. At the same time, this optimization method can obtain the detailed loading conditions and PV irradiance conditions when the line current reaches its maximum value. The extensive tests with different fault resistance at different line locations had been studied to testify the effectiveness of the proposed protection framework. The case study results show that $1.2I_{linemax}$ can be set as the pickup current for overcurrent protection. The expandability has been demonstrated by additional simulation studies in the seven-bus mesh system. Overall, the proposed DE-based overcurrent protection framework is effective to detect the fault and protect the system.

In future work, the hardware-in-the-loop will be conducted to perform real-time simulation of the power system [47–49]. The platform used to execute the proposed framework is OPAL-RT OP5600 equipped in UNSW RTS lab.

Author Contributions: Conceptualization, M.L. and D.Z.; methodology, M.L.; software, M.L.; validation, M.L., S.L. and D.Z.; formal analysis, X.T.; investigation, S.L.; resources, S.L.; writing—original draft preparation, M.L.; writing—review and editing, S.L., X.T. and D.Z.; supervision, T.P. and D.Z.; project administration, D.Z. All authors have read and agreed to the published version of the manuscript.

Funding: This research received no external funding.

Conflicts of Interest: The authors declare no conflict of interest.

References

1. Kakigano, H.; Miura, Y.; Ise, T. Low-Voltage Bipolar-Type DC Microgrid for Super High Quality Distribution. *IEEE Trans. Power Electron.* **2010**, *25*, 3066–3075. [\[CrossRef\]](#)
2. Salomonsson, D.; Soder, L.; Sannino, A. Protection of Low-Voltage DC Microgrids. *IEEE Trans. Power Deliv.* **2009**, *24*, 1045–1053. [\[CrossRef\]](#)
3. Hooshyar, A.; Iravani, R. Microgrid Protection. *Proc. IEEE* **2017**, *105*, 1332–1353. [\[CrossRef\]](#)
4. Tang, X.; Zhang, D.; Chai, H. Synthetical Optimal Design for Passive-Damped LCL Filters in Islanded AC Microgrid. *J. Energy Power Technol.* **2021**, *3*, 22. [\[CrossRef\]](#)
5. Guerrero, J.M.; Loh, P.C.; Lee, T.; Chandorkar, M. Advanced Control Architectures for Intelligent Microgrids—Part II: Power Quality, Energy Storage, and AC/DC Microgrids. *IEEE Trans. Ind. Electron.* **2013**, *60*, 1263–1270. [\[CrossRef\]](#)
6. Smith, M.; Ton, D. Key Connections: The U.S. Department of Energy’s Microgrid Initiative. *IEEE Power Energy Mag.* **2013**, *11*, 22–27. [\[CrossRef\]](#)
7. Tostado-Véliz, M.; Arévalo, P.; Jurado, F. A comprehensive electrical-gas-hydrogen Microgrid model for energy management applications. *Energy Convers. Manag.* **2021**, *228*, 113726. [\[CrossRef\]](#)
8. Faridpak, B.; Alahyari, A.; Farrokhifar, M.; Momeni, H. Toward Small Scale Renewable Energy Hub-Based Hybrid Fuel Stations: Appraising Structure and Scheduling. *IEEE Trans. Transp. Electrification* **2020**, *6*, 267–277. [\[CrossRef\]](#)
9. Lotfi, H.; Khodaei, A. AC Versus DC Microgrid Planning. *IEEE Trans. Smart Grid* **2017**, *8*, 296–304. [\[CrossRef\]](#)
10. Cuzner, R.M.; Venkataramanan, G. The Status of DC Micro-Grid Protection. In Proceedings of the 2008 IEEE Industry Applications Society Annual Meeting, Edmonton, AB, Canada, 5–9 October 2008; pp. 1–8.
11. Nasirian, V.; Moayedi, S.; Davoudi, A.; Lewis, F.L. Distributed Cooperative Control of DC Microgrids. *IEEE Trans. Power Electron.* **2015**, *30*, 2288–2303. [\[CrossRef\]](#)
12. Arunan, A.; Sirojan, T.; Ravishankar, J.; Ambikairajah, E. Real-Time Adaptive Differential Feature-Based Protection Scheme for Isolated Microgrids Using Edge Computing. *IEEE Syst. J.* **2021**, *15*, 1318–1328. [\[CrossRef\]](#)
13. Fletcher, S.D.A.; Norman, P.J.; Galloway, S.J.; Crolla, P.; Burt, G.M. Optimizing the Roles of Unit and Non-unit Protection Methods Within DC Microgrids. *IEEE Trans. Smart Grid* **2012**, *3*, 2079–2087. [\[CrossRef\]](#)
14. Yuan, C.; Haj-ahmed, M.A.; Illindala, M.S. Protection Strategies for Medium-Voltage Direct-Current Microgrid at a Remote Area Mine Site. *IEEE Trans. Ind. Appl.* **2015**, *51*, 2846–2853. [\[CrossRef\]](#)

15. Mohanty, R.; Pradhan, A.K. DC Ring Bus Microgrid Protection Using the Oscillation Frequency and Transient Power. *IEEE Syst. J.* **2019**, *13*, 875–884. [[CrossRef](#)]
16. Beheshtaein, S.; Cuzner, R.M.; Forouzesh, M.; Savaghebi, M.; Guerrero, J.M. DC Microgrid Protection: A Comprehensive Review. *IEEE J. Emerg. Sel. Top. Power Electron.* **2019**, *1*. [[CrossRef](#)]
17. Kumar, D.; Zare, F.; Ghosh, A. DC Microgrid Technology: System Architectures, AC Grid Interfaces, Grounding Schemes, Power Quality, Communication Networks, Applications, and Standardizations Aspects. *IEEE Access* **2017**, *5*, 12230–12256. [[CrossRef](#)]
18. Lu, S.; Ma, R.; Sirojan, T.; Phung, B.; Zhang, D. Lightweight transfer nets and adversarial data augmentation for photovoltaic series arc fault detection with limited fault data. *Int. J. Electr. Power Energy Syst.* **2021**, *130*, 107035. [[CrossRef](#)]
19. Taher, A.M.; Hasanien, H.M.; Ginidi, A.R.; Taha, A.T. Hierarchical Model Predictive Control for Performance Enhancement of Autonomous Microgrids. *Ain Shams Eng. J.* **2021**, *12*, 1867–1881. [[CrossRef](#)]
20. Lopez-Garcia, T.B.; Coronado-Mendoza, A.; Domínguez-Navarro, J.A. Artificial neural networks in microgrids: A review. *Eng. Appl. Artif. Intell.* **2020**, *95*, 103894. [[CrossRef](#)]
21. Alavi, S.A.; Mehran, K.; Vahidinasab, V.; Catalão, J.P.S. Forecast Based Consensus Control for DC Microgrids Using Distributed Long Short-Term Memory Deep Learning Models. *IEEE Trans. Smart Grid* **2021**, *1*. [[CrossRef](#)]
22. Peña-Aguirre, J.C.; Barranco-Gutiérrez, A.I.; Padilla-Medina, J.A.; Espinosa-Calderon, A.; Pérez-Pinal, F.J. Fuzzy Logic Power Management Strategy for a Residential DC-Microgrid. *IEEE Access* **2020**, *8*, 116733–116743. [[CrossRef](#)]
23. Mohanty, R.; Pradhan, A.K. Protection of Smart DC Microgrid With Ring Configuration Using Parameter Estimation Approach. *IEEE Trans. Smart Grid* **2018**, *9*, 6328–6337. [[CrossRef](#)]
24. Meghwani, A.; Gokaraju, R.; Srivastava, S.C.; Chakrabarti, S. Local Measurements-Based Backup Protection for DC Microgrids Using Sequential Analyzing Technique. *IEEE Syst. J.* **2020**, *14*, 1159–1170. [[CrossRef](#)]
25. Yang, J.; Fletcher, J.E.; O'Reilly, J. Short-Circuit and Ground Fault Analyses and Location in VSC-Based DC Network Cables. *IEEE Trans. Ind. Electron.* **2012**, *59*, 3827–3837. [[CrossRef](#)]
26. Cairolì, P.; Dougal, R.A. Fault Detection and Isolation in Medium-Voltage DC Microgrids: Coordination Between Supply Power Converters and Bus Contactors. *IEEE Trans. Power Electron.* **2018**, *33*, 4535–4546. [[CrossRef](#)]
27. Jia, K.; Wang, C.; Bi, T.; Feng, T.; Zhu, R. Transient Current Correlation Based Protection for DC Distribution System. *IEEE Trans. Ind. Electron.* **2020**, *67*, 9927–9936. [[CrossRef](#)]
28. Shabani, A.; Mazlumi, K. Evaluation of a Communication-Assisted Overcurrent Protection Scheme for Photovoltaic-Based DC Microgrid. *IEEE Trans. Smart Grid* **2020**, *11*, 429–439. [[CrossRef](#)]
29. Park, J.; Candelaria, J.; Ma, L.; Dunn, K. DC Ring-Bus Microgrid Fault Protection and Identification of Fault Location. *IEEE Trans. Power Deliv.* **2013**, *28*, 2574–2584. [[CrossRef](#)]
30. Fletcher, S.D.A.; Norman, P.J.; Fong, K.; Galloway, S.J.; Burt, G.M. High-Speed Differential Protection for Smart DC Distribution Systems. *IEEE Trans. Smart Grid* **2014**, *5*, 2610–2617. [[CrossRef](#)]
31. Ara, R.; Khan, U.A.; Bhatti, A.I.; Lee, B.W. A Reliable Protection Scheme for Fast DC Fault Clearance in a VSC-Based Meshed MTDC Grid. *IEEE Access* **2020**, *8*, 88188–88199. [[CrossRef](#)]
32. Reis, M. Optimization of dc feeder rate of rise overcurrent protection settings using delta i cumulative distribution. In Proceedings of the Conference, 2004 IEEE Industrial and Commercial Power Systems Technical, Clearwater Beach, FL, USA, 1–6 May 2004; pp. 63–66.
33. Augustine, S.; Reno, M.J.; Brahma, S.M.; Lavrova, O. Fault Current Control and Protection in a Standalone DC Microgrid Using Adaptive Droop and Current Derivative. *IEEE J. Emerg. Sel. Top. Power Electron.* **2020**, *9*, 2529–2539. [[CrossRef](#)]
34. Emhemed, A.A.S.; Burt, G.M. An Advanced Protection Scheme for Enabling an LVDC Last Mile Distribution Network. *IEEE Trans. Smart Grid* **2014**, *5*, 2602–2609. [[CrossRef](#)]
35. Emhemed, A.A.S.; Fong, K.; Fletcher, S.; Burt, G.M. Validation of Fast and Selective Protection Scheme for an LVDC Distribution Network. *IEEE Trans. Power Deliv.* **2017**, *32*, 1432–1440. [[CrossRef](#)]
36. Baran, M.E.; Mahajan, N.R. Overcurrent Protection on Voltage-Source-Converter-Based Multiterminal DC Distribution Systems. *IEEE Trans. Power Deliv.* **2007**, *22*, 406–412. [[CrossRef](#)]
37. Dragičević, T.; Lu, X.; Vasquez, J.C.; Guerrero, J.M. DC Microgrids—Part II: A Review of Power Architectures, Applications, and Standardization Issues. *IEEE Trans. Power Electron.* **2016**, *31*, 3528–3549. [[CrossRef](#)]
38. Dallago, E.; Liberale, A.; Miotti, D.; Venchi, G. Direct MPPT Algorithm for PV Sources with Only Voltage Measurements. *IEEE Trans. Power Electron.* **2015**, *30*, 6742–6750. [[CrossRef](#)]
39. Moirangthem, J.; Krishnanand, K.R.; Dash, S.S.; Ramaswami, R. Adaptive differential evolution algorithm for solving non-linear coordination problem of directional overcurrent relays. *IET Gener. Transm. Distrib.* **2013**, *7*, 329–336. [[CrossRef](#)]
40. Das, S.; Suganthan, P.N. Differential Evolution: A Survey of the State-of-the-Art. *IEEE Trans. Evol. Comput.* **2011**, *15*, 4–31. [[CrossRef](#)]
41. Fan, Q.; Yan, X. Self-Adaptive Differential Evolution Algorithm With Zoning Evolution of Control Parameters and Adaptive Mutation Strategies. *IEEE Trans. Cybern.* **2016**, *46*, 219–232. [[CrossRef](#)]
42. Gao, Z.; Pan, Z.; Gao, J. A New Highly Efficient Differential Evolution Scheme and Its Application to Waveform Inversion. *IEEE Geosci. Remote Sens. Lett.* **2014**, *11*, 1702–1706.
43. Qin, A.K.; Huang, V.L.; Suganthan, P.N. Differential Evolution Algorithm With Strategy Adaptation for Global Numerical Optimization. *IEEE Trans. Evol. Comput.* **2009**, *13*, 398–417. [[CrossRef](#)]

44. Pan, Z.; Wu, J.; Gao, Z.; Gao, J. Adaptive Differential Evolution by Adjusting Subcomponent Crossover Rate for High-Dimensional Waveform Inversion. *IEEE Geosci. Remote Sens. Lett.* **2015**, *12*, 1327–1331.
45. Mahat, P.; Chen, Z.; Bak-Jensen, B.; Bak, C.L. A Simple Adaptive Overcurrent Protection of Distribution Systems with Distributed Generation. *IEEE Trans. Smart Grid* **2011**, *2*, 428–437. [[CrossRef](#)]
46. Meghwani, A.; Srivastava, S.C.; Chakrabarti, S. A Non-unit Protection Scheme for DC Microgrid Based on Local Measurements. *IEEE Trans. Power Deliv.* **2017**, *32*, 172–181. [[CrossRef](#)]
47. Riccobono, A.; Liegmann, E.; Pau, M.; Ponci, F.; Monti, A. Online Parametric Identification of Power Impedances to Improve Stability and Accuracy of Power Hardware in the Loop Simulations. *IEEE Trans. Instrum. Meas.* **2017**, *66*, 2247–2257. [[CrossRef](#)]
48. Kong, L.; Nian, H. Transient Modeling Method for Faulty DC Microgrid Considering Control Effect of DC/AC and DC/DC Converters. *IEEE Access* **2020**, *8*, 150759–150772. [[CrossRef](#)]
49. Vygoder, M.; Milton, M.; Gudex, J.D.; Cuzner, R.M.; Benigni, A. A Hardware-in-the-Loop Platform for DC Protection. *IEEE J. Emerg. Sel. Top. Power Electron.* **2021**, *9*, 2605–2619. [[CrossRef](#)]